Proceedings of the Seventh International Conference on
Railway Technology: Research, Development and Maintenance
Edited by: J. Pombo
Civil-Comp Conferences, Volume 15, Paper 6.3
Civil-Comp Press, Edinburgh, United Kingdom, 2026
ISSN: 2753-3239, doi: 10.4203/ccc.15.6.3

A Stochastic Dynamics–Based Approach for Rapid Prediction of the Bending Fatigue Life of Mixed Passenger–Freight Railway Frogs

X. Zhu, J. Xu and P. Wang

MOE Key Laboratory of High-speed Railway Engineering, Southwest Jiaotong University, Chengdu, China

Abstract

The concurrent operation of high-speed and heavy-haul services on mixed-traffic railways imposes heightened demands on track structures, particularly the movable point rail of the frog. The complex geometry of the point rail, in conjunction with the significant wheel load transfer, renders the point rail bottom susceptible to fatigue damage under cyclic loading. The present paper integrates a structural finite element turnout model into a multibody system dynamics framework and develops dedicated post-processing procedures for the rapid extraction of stresses in variable-section rails. The investigation builds upon this foundation, systematically examining the spatial distribution characteristics of point rail bottom fatigue life. This is achieved by accounting for the operational patterns of mixed passenger and freight railway, the unique structure of the frog, and the random nature of alternating loads. The research reveals the spatial non-uniformity and probabilistic sensitivity of point rail fatigue, providing innovative engineering methodologies and theoretical foundations for turnout life assessment and high-reliability operations.

Keywords: mixed passenger and freight railway, movable-point frog, vehicle-turnout coupled rigid and flexible model, rail bottom, bending fatigue, probability fatigue life.

1 Introduction

The expansion of railway networks has raised new societal expectations for both daily commuting and freight transport. Convenience, speed, and efficiency are now central objectives in both passenger and freight services [1]. Mixed-use railways operating at speeds of up to 200 km/h are distinguished by their need to accommodate high-speed passenger trains alongside conventional freight traffic. Unlike dedicated passenger or freight-only lines, the design of such hybrid infrastructure must carefully balance the contrasting demands of the two train types. Freight trains impose high axle loads and large carrying capacities, whereas passenger services require high speeds and smooth running conditions. The interaction of these fundamentally different load characteristics results in more complex load patterns than those encountered in single-mode railway systems. As a result, substantially more stringent technical requirements are placed on the rails and the supporting track structure, particularly with respect to load-bearing capacity and long-term durability [2].

Railway turnouts play a crucial role in enabling vehicles to switch between tracks [3], but they also constitute one of the most vulnerable elements of the track system. Wheel–rail impact forces at movable-point frogs are significantly higher than those occurring in the switch region [4]. This is largely due to the complex configuration of movable-point frogs, which consist of numerous components and therefore introduce inherent structural discontinuities. These discontinuities promote wheel load transfer and lead to complex contact conditions, in which a single wheel may simultaneously interact with multiple rails [5]. The combined influence of these factors subjects the point rail and other thin-section rail components to increasingly severe and complex service loads. As illustrated in Figure 1, repeated cyclic loading markedly increases the susceptibility of these components, particularly the point rail, to fatigue damage.

Figure 1: Point rail fatigue fracture of movable-point frog

From the perspective of stress composition, rails are subjected to multiple types of stress during service, including wheel–rail contact stress [6], shear stress [7], bending stress [8], thermal stress [9], and residual stress [10] (see Figure 2). In the frog region, fatigue failure is particularly pronounced in areas not directly exposed to wheel–rail contact. Cracks frequently initiate at the rail bottom and propagate outward, representing the dominant failure mechanism that leads to frog rail fracture [11]. Bending induced by rolling stock loads generates significant tensile stress concentrations in the rail bottom, which constitute a primary driving force for fatigue cracking. The magnitude of rail bottom bending stress depends on several factors, such as train speed and axle load, and is also strongly influenced by the rail section moment of inertia, component stiffness, and mass distribution. Notably, these parameters exhibit inherent uncertainty and variability in practical operating conditions.

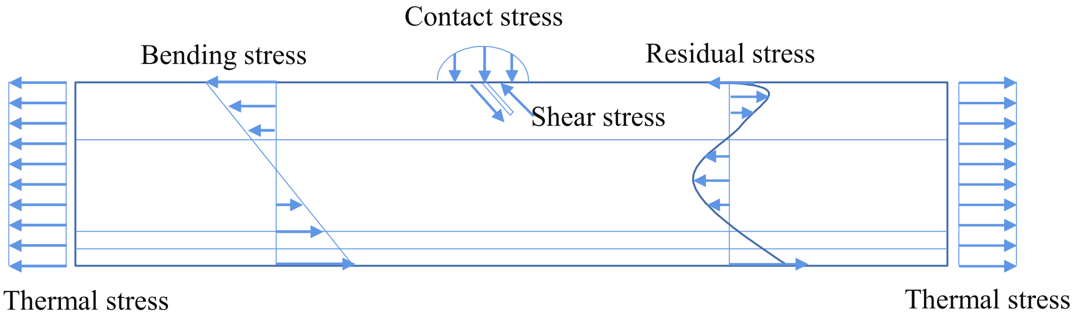

Figure 2: Stress distribution diagram of steel rail

Current research on rail fatigue life predominantly relies on finite element modelling approaches [12–16]. Although these methods provide detailed stress and deformation information, purely finite element–based models suffer from limited computational efficiency. To address this limitation, this study integrates a structural finite element turnout model into a multibody system dynamics framework and develops dedicated post-processing procedures for the rapid extraction of stresses in variable-section rails. This approach provides an efficient methodology for predicting crack initiation life in rails with variable sections. Building on this framework, the study accounts for the operating conditions of mixed passenger and freight railways, the distinctive structural features of movable-point frog, and the stochastic nature of alternating loads during real-world operation. The objective is to systematically analyse the distribution characteristics of bending fatigue life in the rail bottom under the combined influence of random factors.

2 Model description

The CRH2 motor car and the C70 wagon were selected as representative passenger and freight vehicles, respectively. Key system parameters, including mass, inertia, suspension stiffness, and damping, were defined based on design manuals and experimental data from in-service vehicles (see Reference [17]) to ensure realistic simulation results. To balance computational efficiency and accuracy, the vehicle model was simplified by treating the car body, bogies, and wheelsets as rigid bodies, each with six degrees of freedom: translational motion in the X, Y, and Z directions and rotational motion about these axes (yaw, pitch, and roll). This approach preserves the essential dynamic behaviour while significantly improving computational efficiency.

The frog assembly comprises multiple rail components connected by load-transfer devices, fastenings, and the substructure to form an integrated load-bearing system (Figure 3). To enable smooth wheel-load transfer from the wing rail to the point rail, the point rail adopts non-standard sections with continuously varying cross-sectional geometry. As a result, conventional constant-section beam models are inadequate, and variable-section beam models are required. In this study, turnout rails are modelled using Timoshenko beam theory to account for shear deformation and improve stress prediction accuracy. Each rail span is discretised into four beam elements, with constraints applied to longitudinal displacement and rotation about the longitudinal axis to represent realistic boundary conditions. The interaction between rail components and the force-transfer role of jacking blocks and bolts is explicitly considered to ensure effective load transmission and stable operation of movable elements. The baseplate is similarly modelled using Timoshenko beam elements, retaining only vertical displacement and rotation about the x-axis to balance accuracy and computational efficiency. The effects of different fastening arrangements and rail milling methods on stiffness and contact behaviour are also incorporated. Key model parameters are listed in Table 1. Wheel–rail normal contact forces are calculated using Hertzian nonlinear contact theory, while tangential forces are determined using the FASTSIM algorithm to capture creep–slip behaviour and its impact on dynamic response.

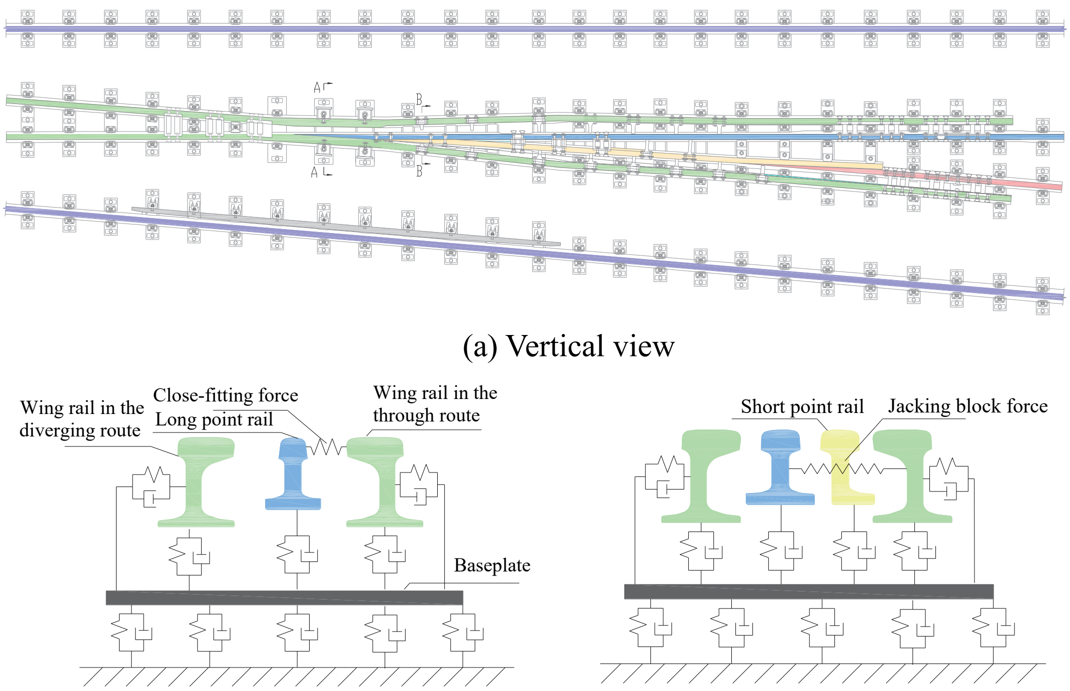

(a) Vertical view

(b) Cross-section A-A

(c) Cross-section B-B

Figure 3: Schematic diagram of the dynamic model of turnout frog area

Parameters		Value and unit
Material properties of steel rails and pads	Young's modulus	214 GPa
	Density	7850 kg/m^3
	Poisson's ratio	0.3
Fasteners	Vertical stiffness of rail pads	300 kN/mm
	Vertical stiffness of plate pads	60 kN/mm
	Lateral stiffness of fasteners	15 kN/mm
Constraint between adjacent rails	Lateral stiffness of the rail head contact	25 kN/mm
	Lateral stiffness of jacking blocks	50 kN/mm
	Vertical and lateral stiffness of bolts	10 MN/mm

Table 1: Parameters of the turnout dynamic model

3 Methods

In this study, bending stresses are derived from bending moments calculated using beam element properties and displacement fields. Nodal displacements of the main structure and substructures, combined with coordinate transformations, are used to reconstruct displacement and acceleration fields in the global coordinate system. The element matrices are exported from the finite element software and simplified under the assumption of small vertical-plane deformations. Based on the resulting response quantities, nodal forces and moments are then directly calculated from the element properties.

$$\begin{bmatrix} F_i \\ M_i \\ F_{i+1} \\ M_{i+1} \end{bmatrix} = \tilde{M}_i \begin{bmatrix} \ddot{u}_{z,i} \\ \ddot{\psi}_i \\ \ddot{u}_{z,i+1} \\ \ddot{\psi}_{i+1} \end{bmatrix} + \tilde{K}_i \begin{bmatrix} u_{z,i} \\ \psi_i \\ u_{z,i+1} \\ \psi_{i+1} \end{bmatrix} \tag{1}$$

In the given context, the variables F_i and M_i are to be interpreted as the nodal forces and nodal moments, respectively. The variables $\tilde{M}_i$ and $\tilde{K}_i$ represent the simplified element mass and stiffness matrix of the element i. It is evident that, in comparison to the effects of stiffness, the inertia terms exert negligible influence on the computational results. Consequently, these terms are disregarded in the analysis.

In the case of a Timoshenko beam, the variation of cross-sectional rotation along the beam coordinate is related to the bending moment according to the following relationship:

$$\frac{\partial \varphi}{\partial x}(x) = -\frac{M(x)}{EI(x)} \tag{2}$$

The bending strain and stress of the rail are, respectively:

$$\varepsilon_i = \frac{\partial \varphi}{\partial x}(x_i) z_i \tag{3}$$

$$\sigma_i = E\varepsilon_i \tag{4}$$

In the formula, ε_i denotes the bending strain, σ_i represents the bending stress, and z_i signifies the perpendicular distance from the rail bottom to the centre of gravity of the cross-section.

The S–N curve derived from rail bending fatigue tests is used as the basis for calculating and evaluating the bending fatigue life of rails. Bending stresses induced by train loading are incorporated into the analysis, and fatigue damage is assessed using Miner’s linear cumulative damage rule. As shown in Figure 4, the S–N curve for 60 kg/m rails is widely adopted in studies of rail bending fatigue life prediction.

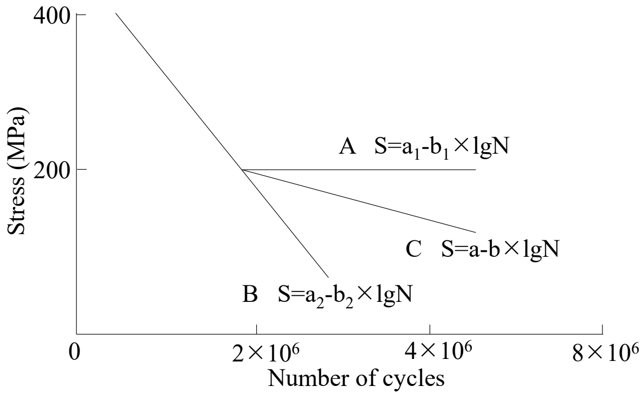

Figure 4: S-N curve of 60kg/m steel rail

The S-N curve formula is as follows:

$$S = a - b\lg N \tag{5}$$

In this equation, *S* denotes the rail bending stress, and *N* represents the number of cycles to fatigue failure. The parameters *a* and *b* are coefficients obtained from the experimentally derived S–N curve. Their values depend on the specified failure probability and are listed in Table 2.

Survival probability (%)	*a*	*b*
99	472.01	48.08
99.9	455.46	48.08
99.99	441.75	48.08

Table 2: Coefficient of S-N curve

It should be noted that thermal and residual stresses reduce the effective mean stress in rails. According to Goodman’s relationship, the influence of mean stress on fatigue life is expressed as follows:

$$\sigma_a = \sigma_{-1}\left(1 - \frac{\sigma_m}{\sigma_b}\right) \tag{6}$$

In the equation, σ_a denotes the stress amplitude, σ_{-1} represents the fatigue limit, σ_m is the mean stress, and σ_b signifies the strength limit. The influence of mean stress, comprising thermal and residual stress, on fatigue life is considered:

$$S = (1 - \frac{\sigma_m}{\sigma_b})(a - b\lg N) \tag{7}$$

where, $\sigma_m = \sigma_t + \sigma_c$, substituting σ_m into the above equation yields:

$$S = (1 - \frac{\sigma_t + \sigma_c}{\sigma_b})(a - b\lg N) \tag{8}$$

From the above equation, *N* is obtained as:

$$N = 10^{\frac{a - \frac{S\sigma_b}{\sigma_b - \sigma_t - \sigma_c}}{b}} \tag{9}$$

The manufacturing of movable-point frog for mixed passenger and freight railway at speeds of 200 km/h and above shall be undertaken using U75VH rail, with a strength limit σ_b of 1180 MPa.

Formula for calculating thermal stress:

$$\sigma_T = E\alpha\Delta T \tag{10}$$

Among these, Young's modulus E = 210 GPa, and the coefficient of thermal expansion $\alpha = 11.5\times10^{-6}$ °C^{-1}. The rail temperature difference ΔT is given by: $\Delta T = T_0 - T$, where T_0 is the stress-free temperature, and T is the current rail temperature. Therefore, $\Delta T > 0$ represents tensile stress. In this paper, it is assumed that $\Delta T = 30$ °C^{-1}, hence $\sigma_T = 72.45$ MPa.

After a certain period of service, the residual stress distribution in rails undergoes significant changes. Tensile stresses on the rail head surface in new rails gradually shift to compressive stresses, while residual stresses in the rail web and bottom largely maintain their original polarity, showing only a relative reduction in magnitude. Studies have shown that repeated high contact stresses gradually relax and diminish residual stresses during operation. Therefore, in the calculation of rail fatigue life, this study neglects the influence of residual stresses on fatigue damage evolution.

Movable-point rail components are subjected to cyclic loading with variable amplitudes. Fatigue life in the time domain can be estimated from the stress or load time history using cycle-counting methods combined with damage accumulation criteria. In this study, the classical Miner linear damage accumulation rule is applied to evaluate the fatigue life of the point rail under multi-stage cyclic loading.

$$D_T = \sum_{i=1}^{k} D_i = \sum_{i=1}^{k} \frac{n_{l,i}}{N_{f,i}} \tag{11}$$

$$T_f = T_0 \frac{1}{D_T} \tag{12}$$

D_T represents total damage from load spectrum cycles; D_i denotes damage induced by loading cycles at the *i*-th stress level; $n_{l,i}$ indicates the number of loading cycles at the *i*-th stress level; $N_{f,i}$ signifies the number of loading cycles at the *i*-th stress level where failure occurs; k denotes the loading stress sequence; T_0 represents the number of load spectrum cycles; T_f denotes total fatigue life.

4 Results

Figure 5 illustrates the bending stress response at the bottom of the point rail during the passage of passenger and freight cars. As shown in Figure 5(a), both vehicle types produce distinct pulsating stress responses, with the maximum bending stress consistently occurring at the 0.647 m cross-section, identifying this location as the critical stress-controlling section of the frog. Freight trains generate significantly higher stress amplitudes due to their larger axle loads, whereas passenger trains produce lower amplitudes but sharper stress pulses with pronounced high-frequency oscillations, reflecting strong dynamic impacts at high speeds. Accordingly, freight loading governs strength design, while passenger loading is critical for fatigue and vibration assessment. Figure 5(b) compares the longitudinal distributions of maximum bending stress along the frog. Both vehicle types exhibit similar unimodal trends; however, within the core stress zone (0.503–0.791 m), freight-induced stresses are consistently higher. At the peak location of 0.647 m, the maximum stress under the freight car reaches 64.57 MPa, approximately 40% higher than the 46.31 MPa observed under the passenger car, underscoring the dominant influence of axle load. In contrast, in the rear section of the frog, passenger cars induce higher bending stresses than freight cars, indicating that high-speed dynamic impacts and vibration effects dominate in this region. Therefore, fatigue design and life assessment of frogs should account for both the maximum stress effects of heavy freight loads and the dynamic fatigue effects induced by high-speed passenger trains.

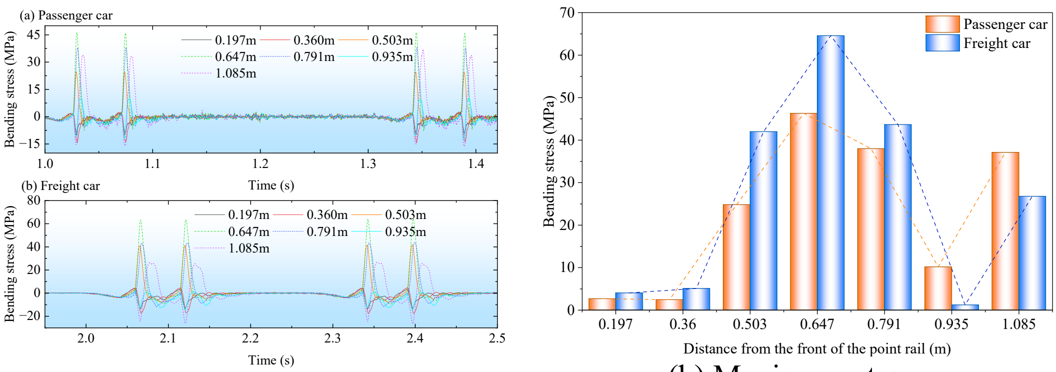

(a) Stress-time curve

(b) Maximum stress

Figure 5: Bending stress of the point rail bottom

As shown in Figure 6, the fatigue life distribution of the point rail bottom is presented for survival probabilities of 99%, 99.9%, and 99.99% under passenger and freight operations. The results indicate pronounced spatial non-uniformity and strong probabilistic sensitivity. Spatially, the fatigue life exhibits a distinct U-shaped distribution, with the minimum life coinciding with the peak bending stress region identified previously. In this critical zone, intense wheel–rail dynamic impacts and abrupt stiffness variations significantly accelerate fatigue damage accumulation, forming a clear fatigue life depression. From a probabilistic standpoint, fatigue life is highly sensitive to reliability requirements. Increasing the survival probability from 99% to 99.99% results in a dramatic, significant reduction in predicted life across all sections. This non-linear behaviour demonstrates that extremely high reliability targets substantially constrain the theoretical service life of the point rail, highlighting the strong influence of stochastic fatigue effects on high-reliability design.

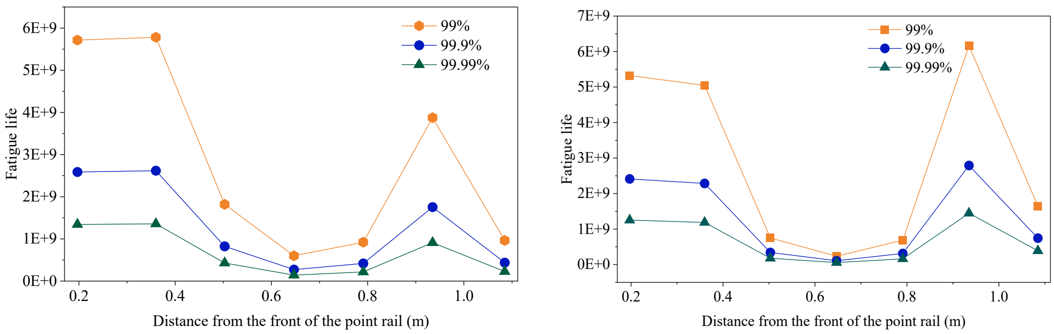

(a) Passenger car (b) Freight car

Figure 6: Fatigue life of the point rail bottom

To capture realistic operational dynamics, parameter variability arising from changes in vehicle mass and suspension stiffness is explicitly considered. Seven key parameters are modelled as random variables: vehicle speed, vehicle mass, vertical and lateral stiffness of the primary and secondary suspensions, and the wheel–rail friction coefficient. Based on test data and engineering experience, all parameters are assumed to follow normal distributions. Their variability is quantified using the coefficient of variation, set to 0.1 for vehicle speed and 0.2 for all other parameters. As shown in Figure 7, bending stress at the bottom of the point rail under random passenger and freight operations exhibits pronounced spatial variation with a non-monotonic, oscillatory pattern, caused by shifts in wheel–rail contact and changes in rail cross-section. The stress distribution is unimodal, with a global maximum at the 0.647 m section. Mean stresses at this location reach 47.45 MPa for passenger trains and 57.28 MPa for freight trains, identifying it as the most critical region for fatigue damage and crack initiation. Stress dispersion increases with stress magnitude, and regions of high stress show greater variability in both box plots and normal distributions. This behaviour reflects the strong influence of random factors such as train speed and axle load, leading to amplified stress fluctuations in critical high-stress zones.

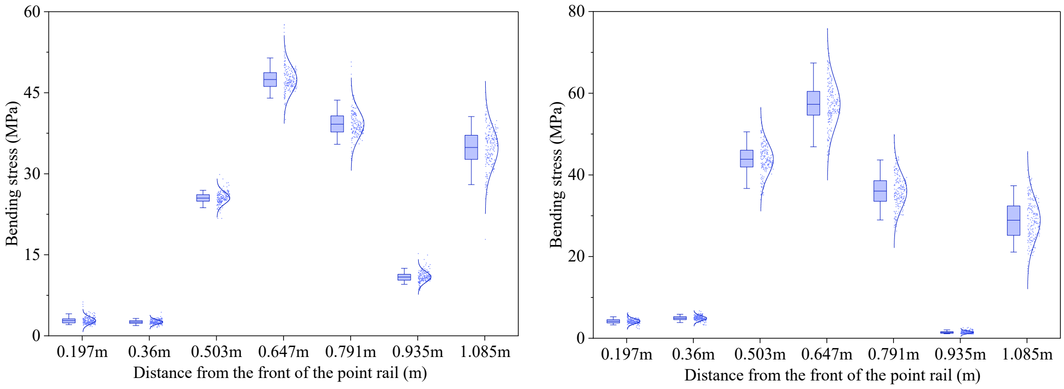

(a) Passenger car (b) Freight car

Figure 7: Distribution of bending stress of the point rail bottom under random operating conditions

Figures 8 and 9 illustrate the fatigue life distribution of the point rail bottom at reliability levels of 99%, 99.9%, and 99.99% under random passenger and freight traffic. The results show that the fatigue life control pattern changes markedly with increasing reliability requirements. Compared with passenger traffic, freight wagons produce a more dispersed fatigue life distribution under identical random conditions, reflecting the pronounced influence of heavy axle loads. As the survival probability increases from 99% to 99.99%, the left tail of the life distribution becomes increasingly dominant, indicating a shift in fatigue control from typical operating conditions to extreme adverse events. Although higher reliability levels lead to a more concentrated overall life distribution, local high-stress regions under freight traffic continue to exhibit substantial life variability. The strong influence of freight train loading further emphasises the need to prioritise heavy-load conditions when addressing extreme fatigue life limitations.

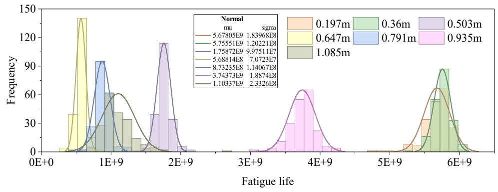

(a) Survival probability 99%

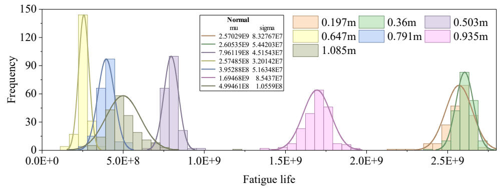

(b) Survival probability 99.9%

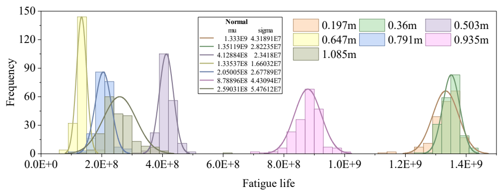

(c) Survival probability 99.99%

Figure 8: The distribution histograms of the fatigue life for the passenger vehicle

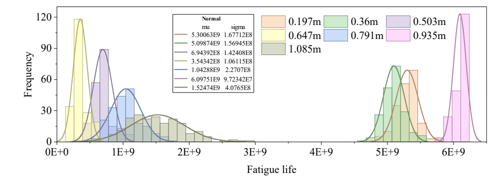

(a) Survival probability 99%

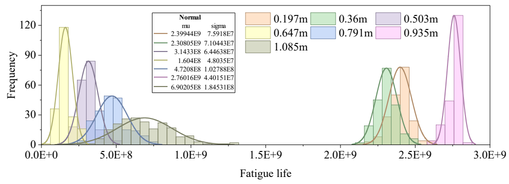

(b) Survival probability 99.9%

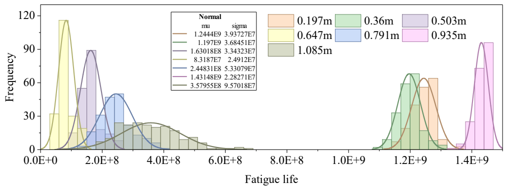

(c) Survival probability 99.99%

Figure 9: The distribution histograms of the fatigue life for the freight vehicle

5 Conclusions and Contributions

This study proposes a probabilistic fatigue life assessment method for turnouts based on a coupled multibody dynamics–finite element approach. The method enables efficient extraction of bending stresses in variable-section rails and fatigue life evaluation under stochastic vehicle loading. The framework characterises the spatial distribution of bending stress at the point rail bottom and the associated fatigue life, providing guidance for frog design and high-reliability operation. The results reveal pronounced pulsating bending stresses in the point rail bottom, with peak stresses consistently located approximately 0.647 m from the front of the point rail. This section is identified as the critical fatigue-vulnerable zone. Combined heavy-load impacts from freight wagons and dynamic shocks from high-speed passenger trains cause significant fatigue life fluctuations in this region. Under random loading, fatigue life exhibits strong spatial non-uniformity and high sensitivity to reliability level. As the survival probability increases from 99% to 99.99%, fatigue control shifts from typical operating conditions to extreme adverse events, with the 0.647 m cross-section remaining the most failure-prone location across all reliability targets.

Acknowledgements

The authors would like thank the support of the National Key R&D Program of China (2023YFB2604305); the National Natural Science Foundation of China (52388102, 52478474, 52122810, 52472458, U23A20666); the Sichuan Science and Technology Program (2024NSFSC0003,2025ZNSFSC1318).

References

[1] S.Q. Li, M.X. Lang, S.Y. Li, et al., "Optimization of High-Speed Railway Line Planning With Passenger and Freight Transport Coordination", IEEE Access, 10, 110217-110247, 2022.

[2] M. Kurhan, D. Kurhan, M. Husak, et al., "Increasing the Efficiency of the Railway Operation in the Specialization of Directions for Freight and Passenger Transportation", Acta Polytechnica Hungarica, 19(3), 231-244, 2022.

[3] J. Yang, M.J. Yue, T.S. Bai, et al., "Analysis of strain rate effect on fatigue crack of fixed frog nose rail", Engineering Fracture Mechanics, 318, 110971, 2025.

[4] P. Wang, Z.H. Zhao, S.Y. Ma, et al., "Evenness improvement method for high-speed turnout crossing areas", Journal of Vibration and Control, 31(5-6), 664-674, 2025.

[5] X.X. Zhu, J.M. Xu, Y. Li, et al., "Load spectrum extrapolation method for fatigue damage of the turnout based on kernel density estimation", Engineering Failure Analysis, 160, 108169, 2024.

[6] L.F. Demisie, M.G. Wedajeneh, A.A. Ejigu, et al., "Effect of compositions and hardness on wheel-rail contact analysis and wear behavior of wheel materials using finite element method: a case study of Addis Ababa light rail transit", Discover Materials, 5(1), 115, 2025.

[7] J.H. Liu, W.Q. Yang, Z.M. Wang, "Fatigue Crack Propagation Analysis of Rail Surface Under Mixed Initial Crack Patterns", Applied Sciences-Basel, 14(23), 11454, 2024.

[8] M.S. Nezhad, F. Larsson, E. Kabo, et al., "Numerical prediction of railhead rolling contact fatigue crack growth", Wear, 530, 205003, 2023.

[9] J.C.O. Nielsen, A. Ekberg, "Probability of rail break caused by out-of-round wheel loads", Engineering Structures, 294, 116717, 2023.

[10] X.Y. Fang, H.N. Zhang, D.W. Ma, et al., "Influence of welding residual stress on subsurface fatigue crack propagation of rail", Engineering Fracture Mechanics, 271, 108642, 2022.

[11] C.J. Hao, X.X. Zhu, W. Wang, et al., "An adaptive multi-axial fatigue model and fatigue damage prediction of the turnout rail", Construction and Building Materials, 472, 140934, 2025.

[12] M. Pletz, W. Daves, H. Ossberger, "A wheel set/crossing model regarding impact, sliding and deformation—Explicit finite element approach", Wear, 294, 446-456, 2012.

[13] Y. Gao, J.M. Xu, Y.B. Liu, et al., "An investigation into transient frictional rolling contact behaviour in a switch panel: validation and numerical simulation", Vehicle System Dynamics, 60(1), 1-18, 2020.

[14] C. Lu, B. Rodríguez-Arana, J.G. Prada, et al., "A Full explicit finite element simulation for the study of interaction between wheelset and switch panel", Vehicle System Dynamics, 58(2), 229-248, 2020.

[15] Q. Yi, X.L. Liu, S.G. Wang, et al., "Failure mechanism and crack propagation behavior of turnout stock rail in high-speed railway", Engineering Failure Analysis, 167, 109026, 2025.
[16] Y. Gao, S.G. Wang, Q. Yi, "Vibration fatigue failure analysis and life prediction of high-speed turnout point rails", Engineering Failure Analysis, 109658, 2025.
[17] X.X. Zhu, Z.H. Zhou, J.M. Xu, et al., "Dynamic performance reliability analysis of mixed passenger and freight railway turnouts based on neural networks", Proceedings of the Institution of Mechanical Engineers, Part F: Journal of Rail and Rapid Transit, 09544097251397469, 2025.